Int. J. Multiphase Flow Vol. 17, No. 3, pp. 309–325, 1991
Printed in Great Britain

0301-9322/91 $3.00 + 0.00
Pergamon Press/Elsevier

PHASE SEPARATION OF DISPERSED MIST AND DISPERSED ANNULAR (RIVULET OR THIN FILM) FLOW IN A TEE—II

ANALYSIS

G. E. McCreery
Idaho National Engineering Laboratory, EG&G Idaho Inc., Idaho Falls, ID 83415, U.S.A.

S. Banerjee
Department of Chemical and Nuclear Engineering, University of California, Santa Barbara, CA 93106, U.S.A.

(Received 19 January 1990; in revised form 3 January 1991)

Abstract—An experimental and analytical investigation of dispersed mist and dispersed annular (rivulet or thin film) flow phase separation in a tee was performed. The analysis portion consisted of developing physically based models and incorporating the models into a computer program that calculates liquid drop and liquid pathline trajectories for these two flow regimes. Macroscopic mass balances were then calculated and compared with data. In addition, a correlation for dispersed mist phase separation was developed from computer calculations and is presented.

Key Words: phase separation, tee, dispersed mist flow, dispersed annular flow

INTRODUCTION

An experimental investigation of phase separation in a tee was presented in part I of this two-part article (McCreery & Banerjee 1990). The observations and data obtained were used to help formulate mechanistically based analytical models of phase separation for dispersed mist and dispersed annular (thin film and rivulet) flow. The work was directed at, but is not specific to, prediction of phase separation in large containment passageways of some CANDU nuclear reactors, as discussed in part I.

This article is a summary of the analytical portion of the research, which is reported in detail in a larger work (McCreery 1988). The literature survey presented in McCreery (1988) indicated that, at the time it was written, only the annular flow phase separation models of Henry (1981), Azzopardi & Whalley (1982) and Azzopardi & Freeman-Bell (1983) were pertinent to either of these two flow regimes. Also, the state of knowledge of the phase separation mechanism was reviewed by Lahey (1986). No model was available for dispersed mist flow. Since that time, several models and correlations for annular flow phase separation have been presented (Sliwicki & Mikielewicz 1988; Shoham *et al.* 1987; Ballyk *et al.* 1988). These models or correlations predict macroscopic mass balances for phase separation, which may then be compared with data. The approach of our research differs in that we modeled trajectories of drops or liquid pathlines and then compared calculated trajectories with experimentally recorded trajectories [a similar approach for phase separation of bubbly flow in a tee was pursued by Lemonnier and Hervieu (1988)]. Once this intermediate step was accomplished and verified, the trajectory models were then implemented in a computer program to calculate the overall mass balances. The mass balances for dispersed mist flow were then compared with our data (no other data are known to exist that may be used for comparison). The final step was to incorporate the calculational results in correlation form. This trajectory mapping approach was possible largely because of our concentration on rectangular cross-section geometry. However, the results for dispersed mist flow are extended for use in circular cross-section, equal flow area pipes by modifying the final correlation to account for geometry.

In this article the models and comparisons of calculations with data for dispersed mist flow are presented first. These sections are followed by a presentation of the dispersed mist flow correlation and then by the models and comparisons of calculations with data for rivulet or thin film flow.

The appendix contains a derivation of the equation relating the slope of a gas streamline at the wall to the adjacent primary flow streamline outside the boundary layer.

DISPERSED MIST FLOW

The basis for calculation of phase separation of dispersed mist flow is the calculation of individual drop trajectories in the gas flowfield. The gas flowfield is modeled as potential flow within the confines of the duct walls and outside the eddy boundaries. The experimental results indicated that the liquid drops exhibit a wide dispersion of sizes (which follow a lognormal distribution), and that drop size is a primary variable in determining drop trajectory. The final mass balance calculation therefore sums individual mass balances for a number of representative drop sizes over the size distribution to arrive at a total mass balance.

The analysis approach chosen was similar to the particle source-in-cell model of Crowe *et al.* (1982), in that the drop trajectory solution was performed using a Lagrangian approach, while the continuous gas phase was calculated by a Eulerian approach. In the general particle source-in-cell model, the flow channel is partitioned into cells and each cell is considered to be a control volume. Finite difference equations describe phasic mass and momentum balances. The drop size distribution is represented by a finite number of drops with several representative diameters. However, we depart from the particle source-in-cell method in several aspects. The departures represent both simplifications and refinements to the method. Major assumptions that permit simplification of drop trajectory and gas flow field equations for many (but not all) typical dispersed mist flows of practical interest are the following:

1. Drop trajectories are unaffected by turbulent fluctuations of the gas. This is a valid assumption for drops with a diameter larger than a few microns (Trela *et al.* 1982), provided that the drops have accelerated to close to gas velocity as discussed in McCreery & Banerjee (1990). Drop diameters of significance for dispersed mist flow are at least an order of magnitude larger. Our experimental data supports this assumption. Drop trajectories are therefore calculated by considering only the mean gas velocity field.
2. The gas flowfield (flow ratio Q_3/Q_1, where Q is volumetric flow rate, 3 is side branch, and 1 is upstream, and streamfunction values) is unaffected by the drop flow and may, therefore, be calculated separately and prior to the calculation of drop trajectories. This assumption is valid for high quality flow. The error in Q_3/Q_1 due to this assumption is estimated in the larger work to be approx. $\pm 4\%$ at a quality (X) of 0.9.
3. Drop interaction (coalescence, breakup and bounding) are ignored. This is a reasonable assumption for high quality flow, as discussed by Crowe (1981).
4. Drop evaporation and condensation are neglected.

In order to accurately calculate mass balances, the concept of "critical" or dividing trajectory, the trajectory for a given drop size that impacts the downstream-side branch corner, was employed. The assumption, which was investigated in our experiments, was then made that all drops of the given size on the side branch side of the critical trajectory exit the side branch, and all drops on the downstream side of the critical trajectory exit the downstream branch. Our experimental results indicate that this assumption is valid for $Q_3/Q_1 \lesssim 0.55$. Above this value, "eddy hopping rivulets", which are described in McCreery & Banerjee (1990), form and the assumption is no longer valid.

The use of critical trajectories, rather than computational cells, for mass balances permits the drop size distribution to be subdivided into a larger number of discrete sizes than would otherwise be possible. The drop size distribution in our model was subdivided into 13 bins rather than only 2 or 3, which is a typical practical limit of the general particle source-in-cell method. The trade-off is that momentum transfer to the gas is not modeled and the results are, therefore, applicable only to high quality flow (i.e. inlet flow quality $\gtrsim 0.85$, as discussed in the larger work).

The gas flowfield was calculated as potential flow bounded by the walls and the corner and downstream eddies. The assumption of potential flow was accurate for the high gas Reynolds numbers encountered in dispersed mist flow, as is shown by our experiments (the correspondence

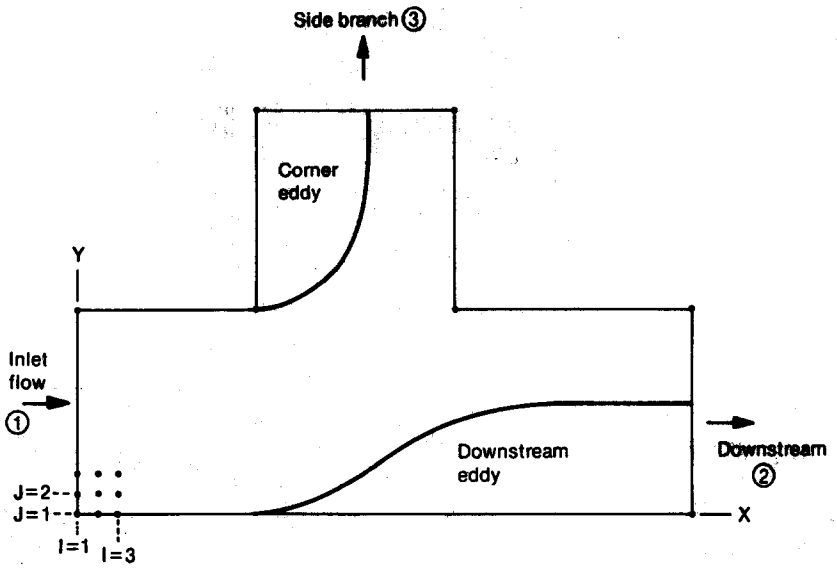

Figure 1. Computer program nomenclature and nodalization.

with potential flow becomes closer as the Reynolds number approaches infinity). The gas flowfield potential flow solution was obtained by solving Laplace's equation numerically in finite difference form. The tee was subdivided into a grid of approx. 8000 square elements, with the grid extending to the vena contracta of the corner and downstream eddies (figure 1). Streamfunction values were calculated at each node using the commonly employed accelerated Gauss–Seidel numerical relaxation technique (Scheid 1968). Streamfunction values at nodes within one node space of the curved eddy boundaries were interpolated from eddy boundary values and nearest neighbor values [the technique of interpolation of degree two as described in Carnahan *et al.* (1969)]. Streamfunction values, when normalized by dividing velocity by upstream velocity, are a function only of Q_3/Q_1 for a given side branch to upstream duct width ratio. Streamfunction values may therefore be calculated and the results stored for later trajectory (or, for thin film or rivulet flow, liquid pathline) calculations at the given gas flow ratio.

The boundary conditions for the potential flow solution are flow ratio Q_3/Q_1 and eddy boundary coordinates (which, in turn, are a function of Q_3/Q_1). The flow was assumed to be uniformly distributed (parallel flow with constant velocities) at the entrance and exits of the computational grid. The maximum widths of the eddies were calculated from their contraction coefficients (minimum flow area divided by duct flow area) obtained from our experimental data or from the free streamline theory values given in McCreery & Banerjee (1990). The corner eddy was modeled as a quarter section of an ellipse (figure 1) with one-half of the major axis length extending to the vena contracta and equaling the side branch duct width in magnitude, as experiments indicate this is a reasonable choice. The downstream eddy was modeled as an S-shaped curve by a fourth-order polynomial (figure 1). With the maximum width of the eddy determined, three experimentally determined values, which were correlated as a function of Q_3/Q_1, specified the initial position of the eddy, the position at which the eddy reaches maximum width, and the skewness of the curve. The use of the above boundary conditions results in a reasonably accurate calculation of potential flow. The accuracy was increased further by fine tuning the downstream eddy position until an additional potential flow boundary condition was satisfied. The additional condition is that the critical gas streamline intersects the downstream-side branch corner at an angle that bisects the 90° corner. This condition arises because the corner is a stagnation point, and the wall containing the corner may be mapped conformally (by the Schwarz–Christofel transformation) into a line upon which stagnation streamlines intersect normally. Streamlines were plotted after calculation by printing a letter or blank for each node depending on streamfunction value (figure 2).

Drop trajectories were calculated after gas flowfield streamfunction values were calculated and stored. Necessary input included: gas inlet velocity; fluid properties; drop diameter (typically the diameter of the average mass drop for each of the 13 bins in the drop diameter distribution); initial

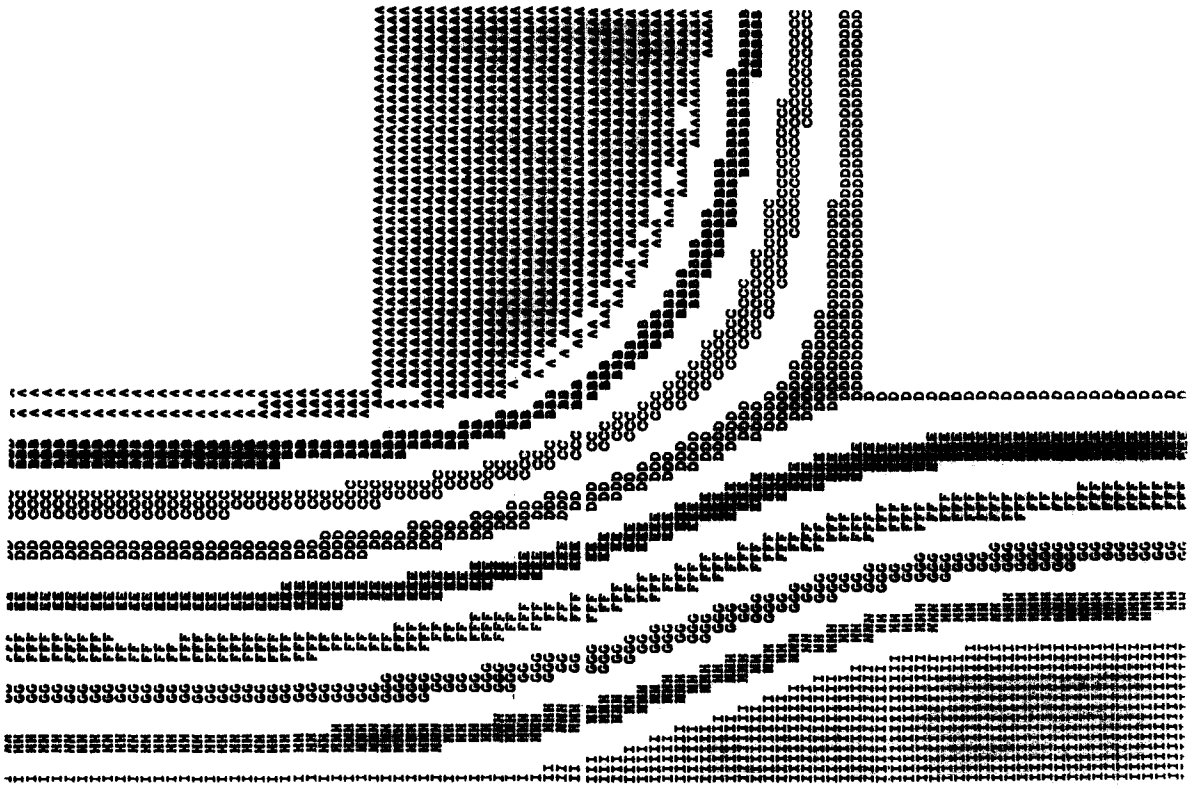

Figure 2. Calculated air streamlines, experiments 1 and 2.

x,y coordinates; and initial drop velocity components V_x and V_y in the x and y directions, respectively (typically $V_x = U$, where U is upstream gas velocity, and $V_y = 0$). A marching solution in time was then employed to calculate drop trajectory coordinates at equal time increments.

The solution proceeds by integration in time of Newton's Second Law,

$$\mathbf{F}_d = m_d \frac{d^2\mathbf{x}}{dt^2}, \qquad [1]$$

where

m_d = drop mass ρ_L 1/6 πd^3,
d = drop diameter,
$\mathbf{x}$ = vector position,
$\mathbf{F}_d$ = vector force on drop,
t = time

and

ρ_L = liquid density.

The force on the drop is given by

$$\mathbf{F}_d = C_d \frac{\pi d^2}{4} \left|\mathbf{V} - \mathbf{V}_d\right| (\mathbf{V} - \mathbf{V}_d), \qquad [2]$$

where

C_d = drag coefficient,

$\mathbf{V}$ = vector gas velocity

and

$\mathbf{V}_d$ = vector drop velocity.

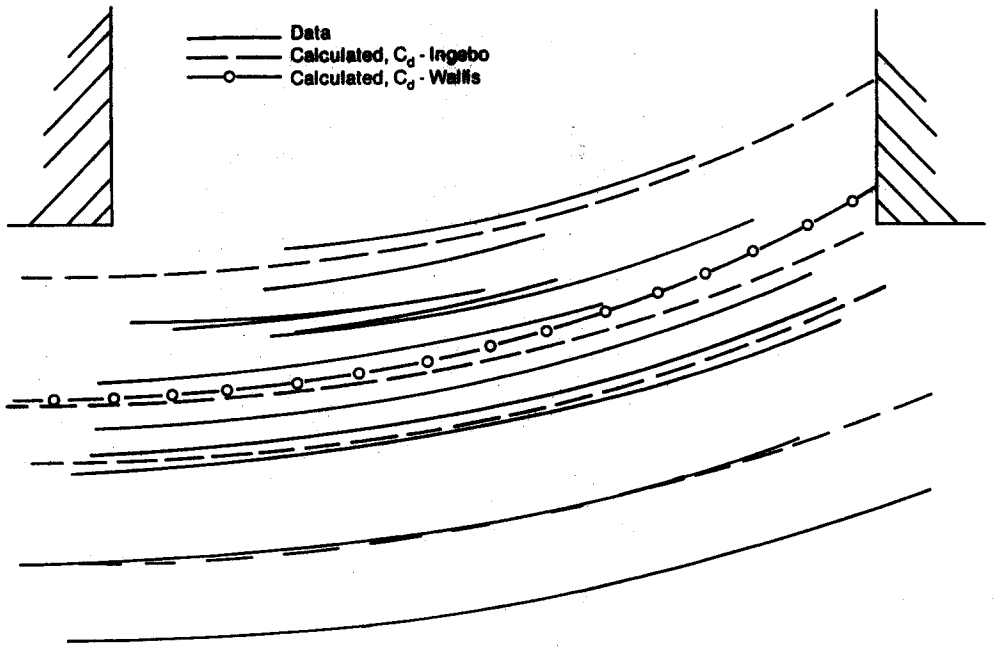

Figure 3. Trajectories of 45 μm latex particles, experiment 3.

The drag coefficient is correlated as a function of drop Reynolds number (Re_d),

$$Re_d = \frac{d|V - V_d|}{\nu}, \quad [3]$$

where

ν = kinematic viscosity.

The drop Reynolds number range of interest for our experiments and for the CANDU geometry was calculated to be approx. 5–500. This represents an intermediate range between laminar Stokes flow ($Re_d < 1.0$) and fully developed turbulent flow ($Re_d > 5{,}000$). Correlations that are reported in the literature to be applicable in this range include Wallis (1969), Clift *et al.* (1978) and Ingebo (1956). Comparisons with our drop and solid particle trajectory (such as shown in figure 3) and trajectory slope data indicate that the Ingebo (1956) correlation best represents our data. The other two correlations are also of acceptable accuracy. The Ingebo correlation is

$$C_d = \frac{24}{Re_d}(1.125\, Re_d^{0.17}). \quad [4]$$

This and the other correlations may be written as

$$C_d = \frac{24}{Re_d} F. \quad [5]$$

If the quantity F varies only slowly with position and marching time increment Δt (which it does), the force balance may be integrated directly to give the drop velocity components

$$V_{xd}(t + \Delta t) = V_x(t) - [V_x(t) - V_{xd}(t)]\exp[-F(t)C \cdot \Delta t] \quad [6]$$

and

$$V_{yd}(t + \Delta t) = V_y(t) - [V_y(t) - V_{yd}(t)]\exp[-F(t)C \cdot \Delta t], \quad [7]$$

where

$$C = \frac{18\nu\rho_G}{\rho_L d^2}. \quad [8]$$

The gas velocity at each position was obtained from the derivatives of the streamfunction value at the position with x and y. The local streamfunction value at each position was obtained by interpolation from nearest grid point neighbor values.

These equations were integrated once more with time to calculate the drop position. An error estimate for position was obtained by comparing the drop position from the integrated equation with that from the simple predictor–corrector value of drop position at time t, plus the average of the new and old time step velocity multiplied by the time increment. This error was close to zero if at least 50 time increments were used to traverse the side branch duct width.

The critical drop trajectory was calculated by first inputting an estimated initial position. The code then calculated this trajectory and impact position. The code then readjusted the initial position until the impact position was sufficiently close to the corner (within 0.005 duct width).

Once the initial position ordinates (y_{0i}, $i = 1$ to 13) for the average mass drops for each of the 13 bins of the size distribution were determined, they were combined to evaluate macroscopic mass balances. The liquid mass flow rate entering the downstream branch is calculated as

$$\dot{m}_{L2} = \frac{\dot{m}_{L1} \sum_{i=1}^{13} f_{mi} y_{0i}}{W_1}, \qquad [9]$$

where

$$f_{mi} = \text{mass fraction of drops in bin } i, \ \sum_{i=1}^{13} f_{mi} = 1, \qquad [10]$$

$$W_1 = \text{upstream duct width}$$

and

$$\dot{m}_{L1} = \text{upstream liquid mass flow rate.}$$

With this value determined and the upstream liquid mass flow rate and the gas mass flow rates known, side branch and downstream mass flow rates and qualities were calculated directly from continuity.

CALCULATED MACROSCOPIC BALANCES COMPARED WITH EXPERIMENTAL DATA

Macroscopic balances were calculated for experiments 1 and 2, and are given in table 1 of part I of this article series (McCreery & Banerjee 1990). These two experiments (which were repeated several times each) are the experiments of acceptable accuracy for which the flow ratio Q_3/Q_1 is less than the ratio of 0.55 above which liquid is transferred from the downstream eddy to the corner eddy. The results of the calculations for the liquid separation ratio, $(1 - X_3)/(1 - X_1)$, were compared with data in table 1.

The accuracy of the calculated liquid separation ratio was determined primarily by the accuracy of drop trajectories, the accuracy of determining the drop diameter distribution, the gas flow ratio and inlet velocity. In our experiments the last two quantities are accurately measured. The drop diameter distribution accuracy was approx. $\pm 6\%$, and the trajectory accuracy was approx. $\pm 5\%$. The accuracy of the liquid separation ratio may be estimated by varying these last two quantities in a sensitivity calculation. The accuracy of the calculation was approx. ± 0.02, which is similar to the accuracy of the experiment. For situations where $(1 - X_3)$ is larger, such as for flow in larger ducts, the accuracy of the calculated liquid separation ratio will be approximately the same, and therefore, on a percentage basis, the error will be less.

Table 1. Liquid separation ratio, experiments 1 and 2

Experiment	$\frac{(1 - X_3)}{(1 - X_1)}$ Calculated	Data
1	0.057	0.07 ± 0.025
2	0.048	0.055 ± 0.025

CORRELATION FOR LIQUID SEPARATION RATIO FOR EQUAL DUCT WIDTH TEES

A correlation for the liquid separation ratio, $(1 - X_3)/(1 - X_1)$, was developed from computer code calculations. The liquid separation ratio was correlated as a function of the upstream velocity U (m/s), duct width W (m) and gas density ρ_G (kg/m^3). (Attempts to nondimensionalize the correlation were not successful because the drop size distribution and drop drag coefficient have different and nonlinear dependences on the gas velocity.) The liquid density was assumed to be that of water at 93°C. The correlation is applicable for either air–water or steam–water flow with gas density between 0.56 and 1.92 kg/m^3 (duct pressure is therefore on the order of 1 bar). Drops were assumed to be formed by entrainment in the upstream duct. Gas viscosity exhibited only a very small influence on the calculations and was therefore fixed at a value representative of saturated steam at 1 bar pressure, which was approximately equal to that of air at 93°C. The gas velocity range was from 20 to 200 m/s. The lower gas velocity was, in general, too low to entrain a large fraction of liquid flow as drops, but was employed in the correlation as a lower limit to provide symmetry to the curves.

The most surprising feature of the calculations was that the liquid separation ratio was only a weak function of the gas flow ratio for ratios below 0.55 (the gas flow ratio is therefore not included in the correlation). This occurred because of the form of the liquid separation ratio. $(1 \times X_3)$ does not vary significantly with the gas flow ratio because the initial ordinates of critical drop trajectories vary approximately linearly with Q_3/Q_1, with all other quantities held constant. This in turn occurs because the drag coefficients for the same size drops do not vary significantly with Q_3/Q_1 for the same upstream gas velocity (individual drop trajectory calculations confirm this assessment).

The correlation is as follows:

$$Y = \frac{1 - X_3}{1 - X_1} = Y_{20} + A_1 \cdot Z^4 + A_2 \cdot Z^3 + A_3 \cdot Z^2, \qquad [11]$$

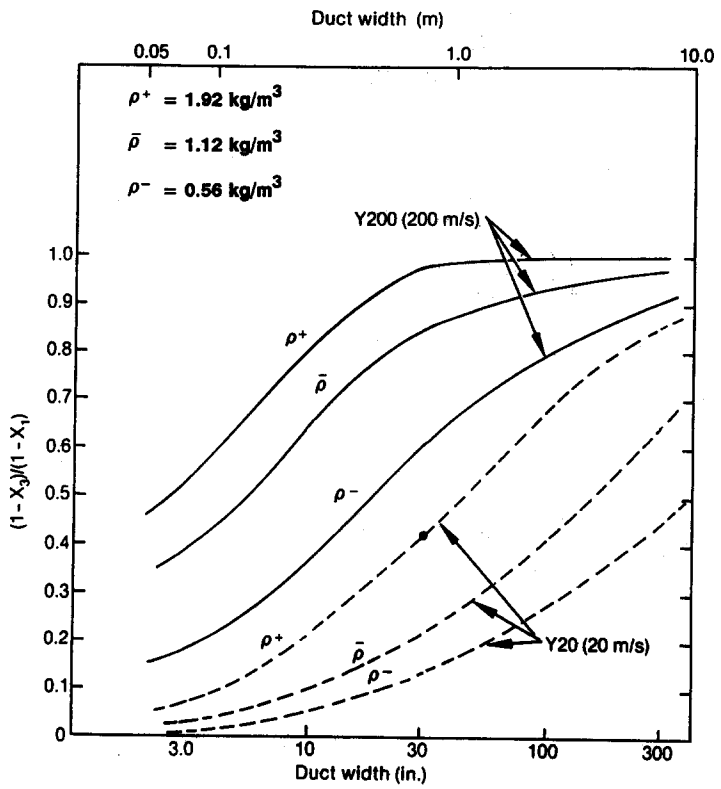

Figure 4. Calculated liquid separation ratio at 20 and 200 m/s, upstream velocity vs duct width.

where

$$Z = U - 20, \tag{12}$$

$$A_1 = \frac{H \cdot (-3 + A_5)^4}{A_4}, \tag{13}$$

$$A_2 = \frac{H \cdot (4 - 2 \cdot A_5)}{A_4^3}, \tag{14}$$

$$A_3 = \frac{H \cdot A_5}{A_4^2}, \tag{15}$$

$$A_4 = 180\ (= 200\ \text{m/s} - 20\ \text{m/s}), \tag{16}$$

$$A_5 = \frac{\left(\frac{A_6^4}{2}\right) - 1}{(A_6 - 1)^2} - \frac{4}{A_6 - 1}, \tag{17}$$

$$A_6 = 17 \cdot \left(\frac{W}{3}\right)^{0.12} \cdot (\rho_G \cdot 0.06243 + 0.03826), \tag{18}$$

$$W = \text{duct width (m)} \cdot 0.0254\ [= \text{duct width (in.)}] \tag{19}$$

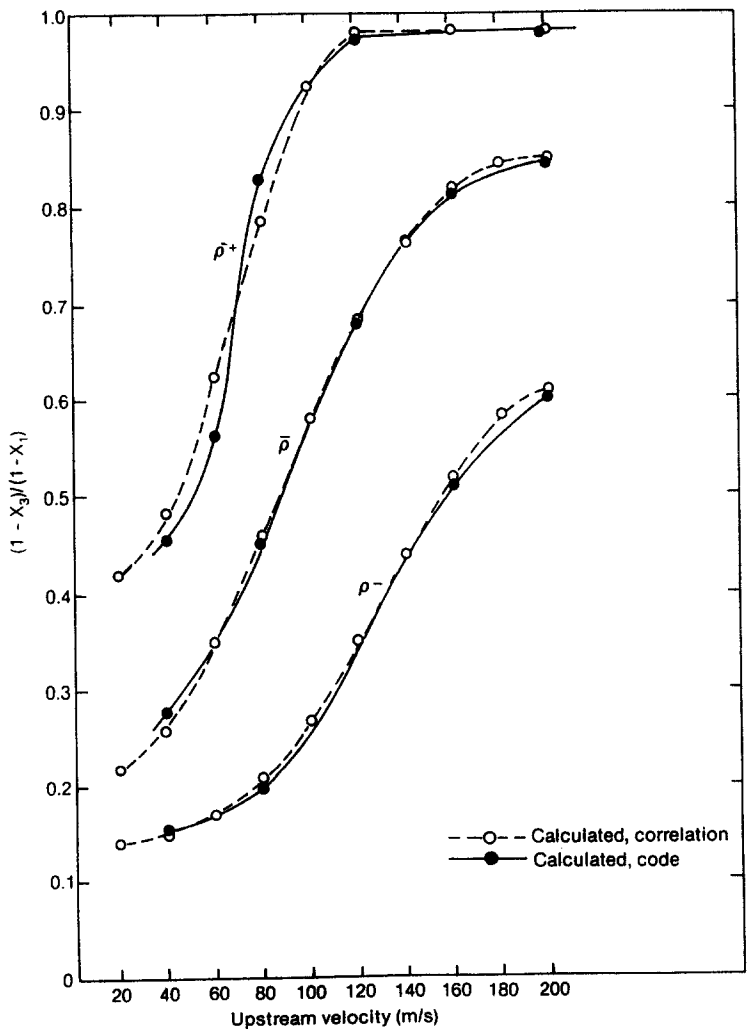

Figure 5. Calculated liquid separation ratio vs upstream velocity for duct width = 0.78 m.

and

$$H = Y_{200} - Y_{20}, \quad [20]$$

$$\text{if } Y > Y_{200}, \text{ then } Y = Y_{200}. \quad [21]$$

$$\text{if } Y < Y_{20}, \text{ then } Y = Y_{20}. \quad [22]$$

Values of Y_{200} and Y_{20} are obtained from figure 4.

Values of the liquid separation ratio calculated using the correlation are compared with the computer calculations in figure 5, for a duct width of 0.78 m. The accuracy of the correlation in predicting the computer calculations was similar for the other two duct widths examined (0.076 m, which represents our experimental apparatus; and 8.0 m, which represents the CANDU reactor passagway of interest), and was at worst ± 0.07. This value, combined with the possible error due to drop diameter distribution uncertainty (described in the larger work) of ± 0.04, gave an RMS uncertainty for the correlation of approx. ± 0.08 at the higher gas density and ± 0.05 at the medium and lower densities.

EXTENSION OF THE CORRELATION FOR CIRCULAR CROSS-SECTION DUCTS

The correlation for the liquid separation ratio for rectangular cross-section ducts may be extended to circular cross-section pipes with equal main and branch diameter in a simple fashion if the following two assumptions are made: (1) the gas velocity and drop number density are uniform across the upstream duct; and (2) the gas flowfield is described by geometrically self-similar potential flow fields at any plane bisecting the three branches of the duct and parallel to the plane described by the axes of the three pipe branches (note that the assumption of equal upstream, downstream and side branch width is maintained in any such plane). If these assumptions are made, then the liquid separation ratio may be calculated by the cross-section area weighted average of the individually calculated liquid separation ratios for each area. The individual calculations are made using the duct width that passes through the centroid of each area.

As an example, the duct cross-section is subdivided into the three equal area segments a, b and c, as shown in figure 6. The representative duct widths in each segment, W_a, W_b and W_c, are chosen as the widths that pass through the centroid of each segment. For three equal area segments,

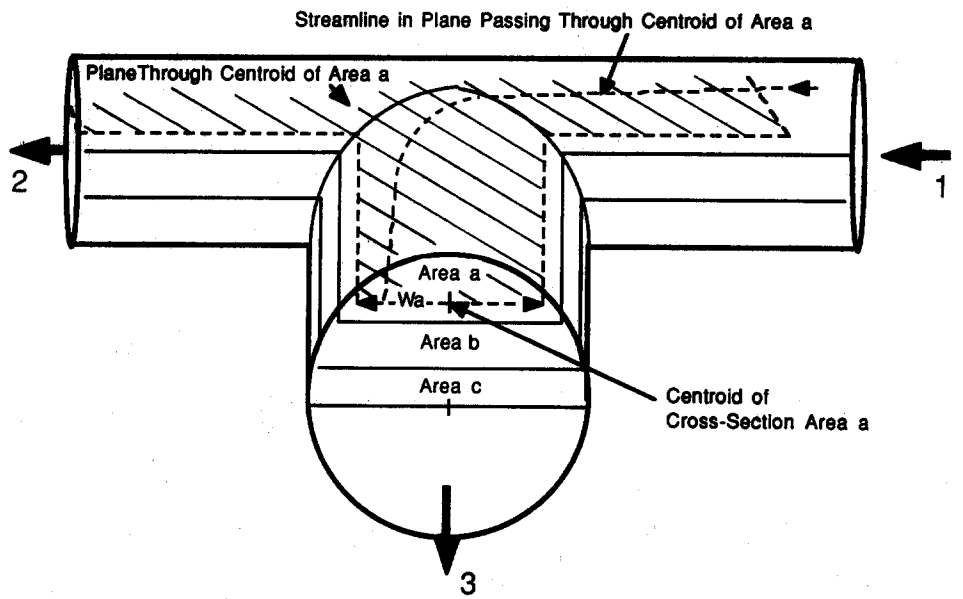

Figure 6. Circular pipe geometry and nomenclature for use in the correlation.

$W_a = 0.675 \cdot D$, $W_b = 0.915 \cdot D$ and $W_c = 0.99 \cdot D$, where D is the pipe diameter. The liquid separation ratio is then

$$Y = (1/3) \cdot (Y_a + Y_b + Y_c), \quad [23]$$

where the three values Y_a, Y_b and Y_c are the separation ratios calculated individually from the correlation using the three appropriate widths. The calculated side branch quality X_3 is always slightly higher than the value for a rectangular duct with width equal to pipe diameter. Because the accuracy of extending the correlation to circular cross-section pipes is unknown (no data exists with which to compare it), but is undoubtedly less than that for a rectangular cross-section duct, subdividing the pipe into more than three segments for the calculation is probably unwarranted.

RIVULET OR THIN FILM FLOW

A liquid rivulet or thin film element attached to the upper or lower wall of a rectangular cross-section tee follows a path that diverges from the gas streamlines of the bulk flow, as described in part I (McCreery & Banerjee 1990). The path of the rivulet or thin film element was seen experimentally to follow the air streamlines at the walls if the liquid momentum was small compared with the gas momentum (liquid momentum per unit volume in our experiments, as calculated from measured rivulet velocity, was always <0.1 of gas momentum per unit volume). Gas velocities, and therefore streamlines, in the boundary layer close to the walls were determined by the sum of primary and secondary flow components. The primary flow followed the streamlines of the bulk flow, but its velocity varied with the distance from the wall. Because both primary and secondary velocity components go to zero at the wall, the streamlines at the wall were calculated by the asymptotic solution method derive in the appendix. The method relates the slope of a streamline at the wall to the slope of the bulk flow streamline at the same x, y position.

The solution of liquid pathline coordinates started at an initial position upstream of the tee and marched along the pathline. At each position the local gas velocity components were first calculated for the bulk flow from potential flow streamfunction values, as was done for dispersed mist flow. Next, the local radius of curvature (R) of the primary streamline was calculated from the following equation (Wardle 1965):

$$\frac{1}{R} = \frac{\dfrac{d^2y}{dx^2}}{\left[1 + \left(\dfrac{dy}{dx}\right)^2\right]^{3/2}}, \quad [24]$$

where x and y are the local primary streamline coordinates (see the appendix, figure A1). The first and second derivatives were calculated in centered finite difference form. Next, the local slope of the wall streamline with respect to the bulk flow streamline ($\tan \alpha$) was calculated from the final equation given in the appendix. For an accurate calculation, the initial position of the path must be in a region of zero streamwise vorticity (zero streamline curvature). A distance of approximately one side branch duct width upstream of the side branch entrance is sufficient to ensure this. After the slope was calculated, the liquid path was advanced one increment in this direction, the slope recalculated and the initial liquid path advanced along a line with the average of the two slopes (a simple predictor–corrector technique).

CALCULATED LIQUID PATHLINES COMPARED WITH DATA

Rivulet pathlines are plotted in figure 7 for experiments 1 and 2 (the pathlines are the same because only the upstream velocity and not the flow ratio varies in the two experiments) and in figure 8 for experiment 3. Both calculated and recorded pathlines are presented along with primary flow streamlines. The calculations predict the data quite well except in the vicinity of the downstream-side branch corner where the vorticity becomes very large due to the decreasing radius of curvature of the primary streamlines. The calculated pathlines approach the corner more closely than in reality before veering off. This is due primarily to the assumption of two-dimensional primary flow that is not correct in this region. In any case, the accuracy of the pathline calculation

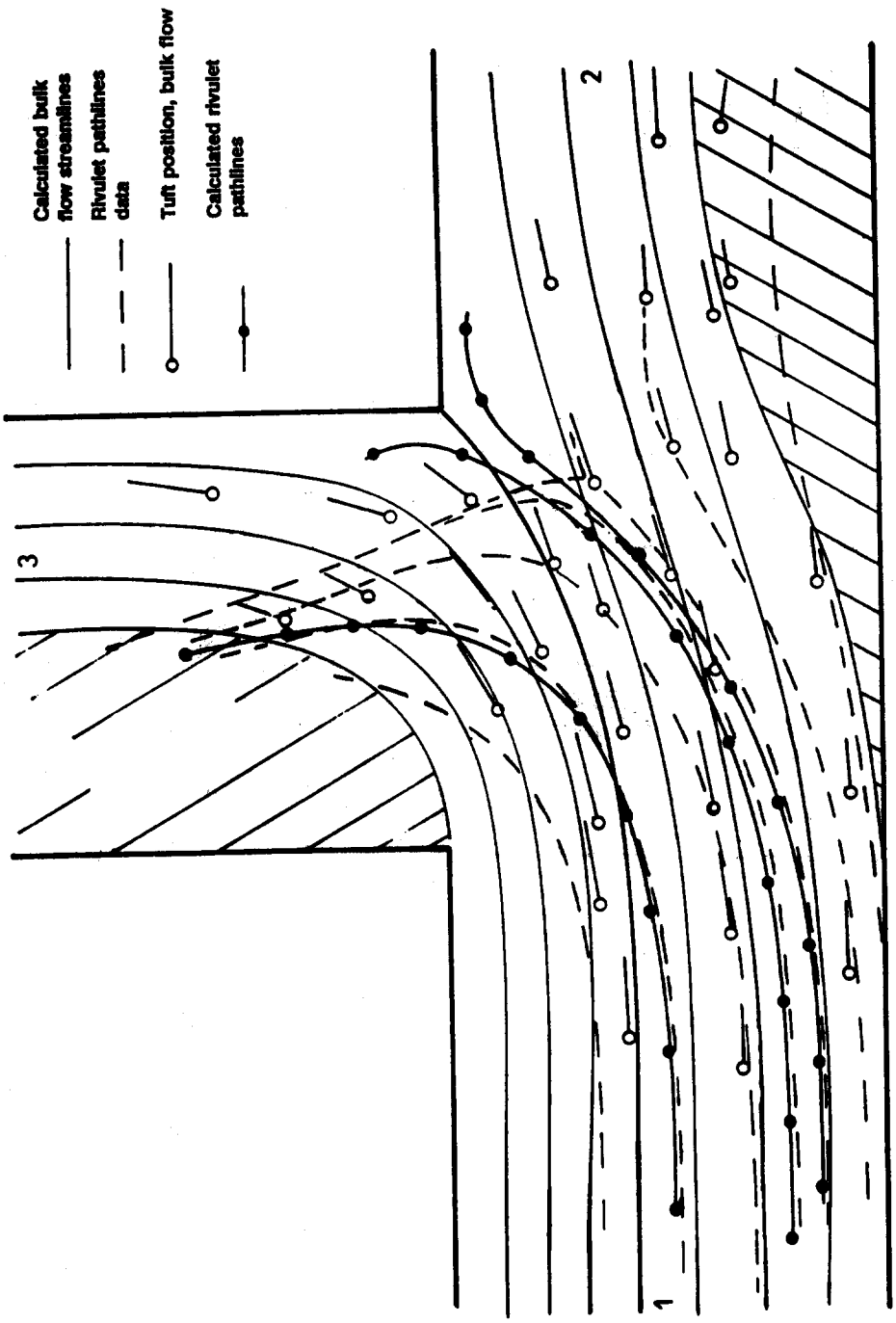

Figure 7. Rivulet pathlines, experiments 1 and 2.

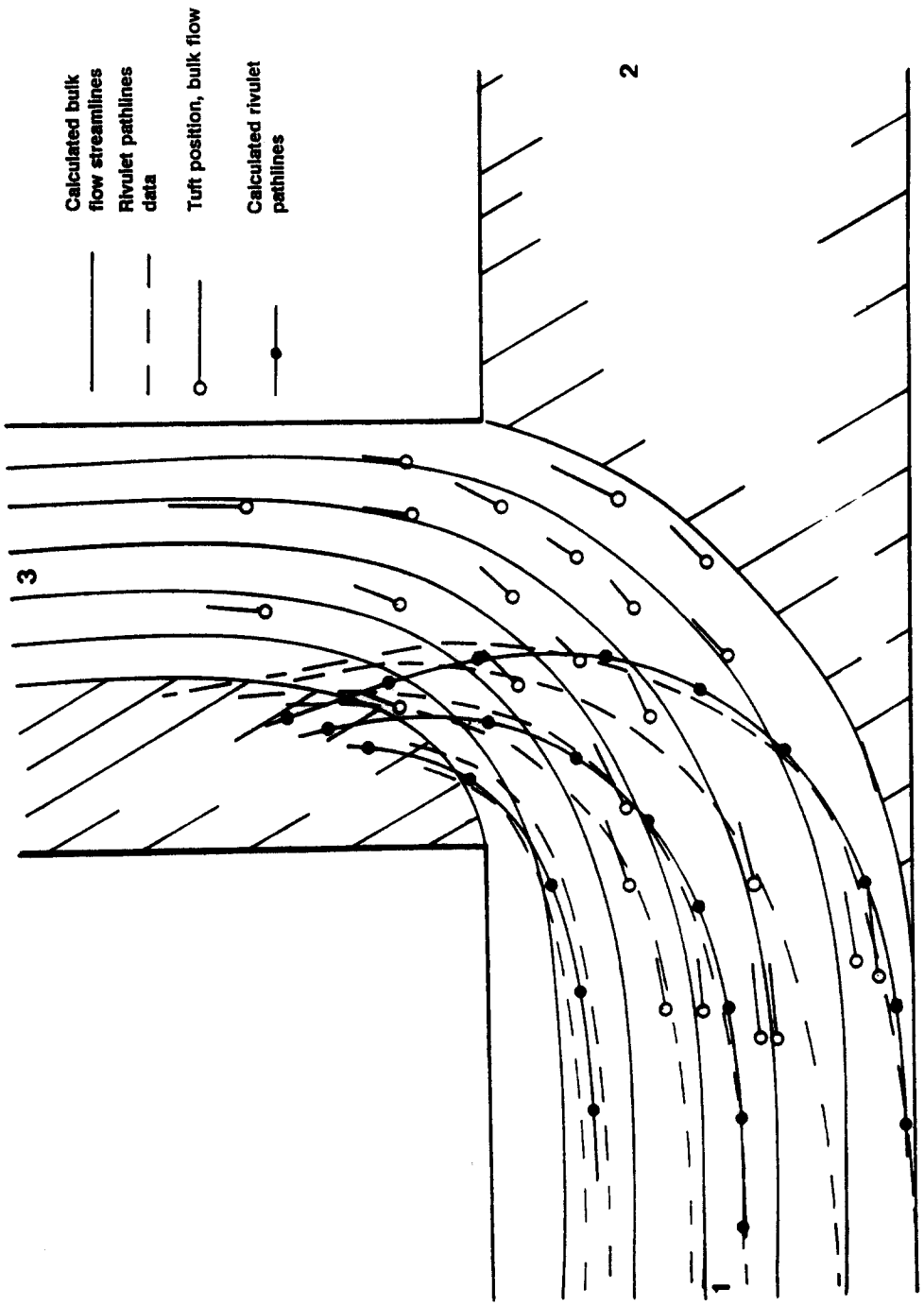

Figure 8. Rivulet pathlines, experiment 3.

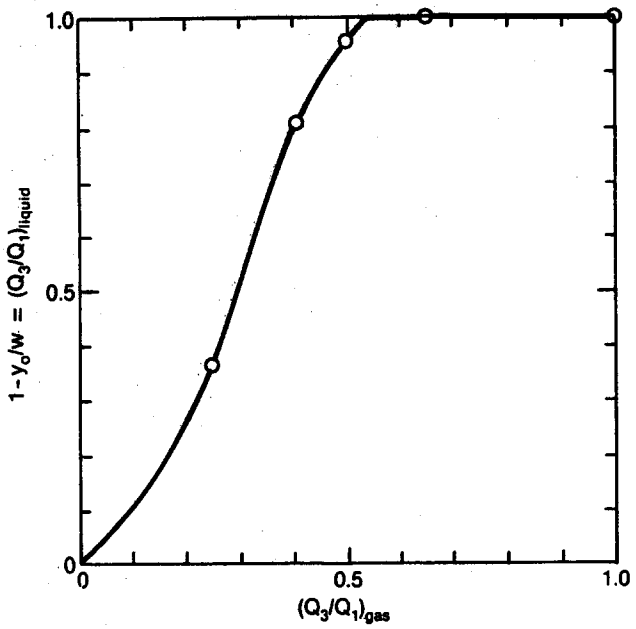

Figure 9. Calculated rivulet or thin film liquid flow ratio for uniform liquid distribution on the top or bottom wall for equal duct widths.

near the corner has little effect on the calculation of the initial ordinate position of the critical pathline, the pathline that divides the flow into side branch and downstream components, and is, therefore, of primary importance for phase separation calculations. The accuracy of calculating the initial ordinate of a critical pathline is approx. $\pm 5\%$ of duct width.

Consistent with the explanation of eddy hopping rivulets [given in McCreery & Banerjee (1990)], critical pathlines only exist for $Q_3/Q_1 < 0.55$ (cf. figure 7 with figure 8). The critical pathline is a "virtual pathline" for rivulet or thin film flow because the liquid is always observed experimentally to veer away from the corner before impacting it.

The liquid separation ratio and other macroscopic balances for rivulet or thin film flow may be easily calculated from known inlet conditions, including the liquid distribution along the walls and the gas flow ratio, if the critical pathline initial ordinate is known. It is plotted in normalized form in figure 9 as a function of the gas flow ratio. It is interesting to observe that the primary variable for determining the phase separation for rivulet or thin film flow is Q_3/Q_1, while the upstream gas velocity and duct width play no part. This is the exact opposite as compared with dispersed mist flow. For dispersed annular flow all of these variables should prove to be of importance (along with the film thickness and film distribution for thick film dispersed annular flow). For the special case of dispersed annular flow with a thin evenly distributed film, the correlation for the dispersed mist liquid separation ratio may be used for the dispersed mist component, and figure 9 may be used to calculate the liquid flow on the wall component and the results combined.

CONCLUSIONS

An analytical investigation of dispersed mist and dispersed annular (rivulet or thin film) phase separation in a tee resulted in the development of computer models that describe liquid drop trajectories for dispersed mist flow and liquid pathlines for rivulets or thin films. Computer predictions were then compared with data obtained in the experimental portion of the research. Other data compared included gas streamlines, eddy boundaries and macroscopic mass balances. The process of comparison provided accuracy estimates for the models.

Dispersed mist flow is characterized by a wide dispersion of drop sizes, with the drop size being a primary variable in determining the drop trajectory. It was therefore necessary to calculate a number of representative drop size trajectories (typically 13 individual sizes) in order to accurately calculate macroscopic mass balances. The concept of a critical, or dividing, trajectory was employed

in the calculations, which is valid for gas flow ratios <0.55. Above this ratio eddy hopping rivulets form and liquid is transferred directly from the downstream eddy to the side branch corner eddy, and the concept no longer remains valid. The gas flow ratio above which eddy hopping rivulets occur in circular cross-section pipes is not yet known but, because secondary flow is qualitatively similar in rectangular and circular cross-section pipe tees, the phenomenon surely exists and should be considered in phase separation models.

The dispersed mist macroscopic mass balance calculations were used to develop a correlation for the liquid separation ratio for steam–water or air–water flow at near atmospheric pressure conditions. The liquid separation ratio was formulated as a function of the primary variables involved including gas density, duct width and upstream velocity. Somewhat surprisingly, gas flow ratio, Q_3/Q_1, was not a significant variable (except that it must be <0.55 for the correlation to be valid). This is due to the nondimensional form of the liquid separation ratio. The correlation may be extended to pipes of circular cross-section by a simple algorithm.

Rivulet and thin film pathlines were observed experimentally to follow the gas streamlines at the wall. Therefore, the calculation of the liquid pathline along the wall involves solely the calculation of gas streamlines at the wall (only if liquid momentum is small compared with gas momentum). An asymptotic method was developed to predict the slope of the streamline at the wall compared with the streamline of the adjacent bulk flow. A marching solution provides the pathline trajectory. The method is reasonably accurate and also correctly predicts the eddy hopping rivulet trajectories for dispersed mist flow (the phenomena occurs because of secondary flow along the walls). How to calculate the flow rate of these rivulets is not yet known. Rivulet or thin film pathlines and macroscopic balances are shown to depend primarily on the gas flow ratio.

Acknowledgements—We wish to thank Ontario Hydro, and specifically W. I. Midvidy, for providing financial and technical support for this research. We also thank Professors H. Fenech and T. G. Theofanous for helpful and stimulating discussions.

This work was performed in part under the auspices of the U.S. Department of Energy, DOE Contract No. DE-AC07-76ID01570.

REFERENCES

AZZOPARDI, B. J. & FREEMAN-BELL, G. 1983 The effects of side arm diameter on the two phase flow split at a T-junction. Report AERE-M3290.

AZZOPARDI, B. J. & WHALLEY, P. B. 1982 The effect of flow patterns on two-phase flow in a T-junction. *Int. J. Multiphase Flow* **8,** 491–507.

BALLYK, J. D., SHOUKRI, M. & CHAN, A. M. C. 1988 Steam–water annular flow in a horizontal dividing T-junction. *Int. J. Multiphase Flow* **14,** 265–285.

CARNAHAN, B., LUTHER, H. & WILKES, J. 1969 *Applied Numerical Methods*. Wiley, New York.

CLIFT, R., GRACE, J. R. & WEBER, M. E. 1978 *Bubbles, Drops, and Particles*. Academic Press, New York.

CROWE, C. T. 1981 On the relative importance of particle–particle collisions in gas–particle flows. Presented at the *Conf. on Gas Borne Particles*, Inst. of Mech. Engrs, Oxford, Paper C78-81.

CROWE, C. T. 1982 Review—Numerical models for dilute gas–particle flows. *J. Fluids Engng* **104,** 297–302.

CROWE, C. T., SHARMA M. P. & STOCK, D. E. 1977 The particle-source-in-cell (PSI-CELL) model for gas–droplet flows. *J. Fluids Engng*. **99,** 325–332.

CURRIE, I. G. 1974 *Fundamentals of Fluid Mechanics*. McGraw-Hill, New York.

HAWTHORNE, W. R. 1951 Secondary circulation in fluid flows. *Proc. R. Soc.* **A206,** 374–387.

HENRY, J. A. R. 1981 Dividing annular flow in a horizontal tee. *Int. J. Multiphase Flow* **7,** 343–355.

HORLOCK, J. H. & LAKSHMINARAYANA, B. 1973 Secondary flows: theory, experiment, and application in turbomachinery aerodynamics. *A. Rev. Fluid Mech.* **5,** 247–280.

INGEBO, R. D. 1956 Drag coefficients for droplets and solid spheres in clouds accelerating in air streams. Report NACA-TN 3762.

LAHEY, R. T. JR 1986 Current understanding of phase separation mechanisms in branching conduits. *Nucl. Engng Des.* **7**, 342–355.

LEMONNIER, H. & HERVIEU, E. 1988 Theoretical modelling and experimental investigation of single-phase and two-phase flow division at a T-junction. In *ANS Proc. 1988 natn. Heat Transfer Conf.*, Houston, Tex.

MCCREERY, G. E. 1988 Investigation of dispersed and dispersed-annular (rivulet or thin film) flow phase separation in tees. Ph.D. Dissertation, Dept of Chemical and Nuclear Engineering, Univ. of California, Santa Barbara, Calif.

MCCREERY, G. E. & BANERJEE, S. 1990 Phase separation of dispersed mist and dispersed annular (rivulet or thin film) flow in a tee—I. Experiments. *Int. J. Multiphase Flow* **16**, 429–446.

SCHEID, F. 1968 *Theory and Problems of Numerical Analysis*. McGraw–Hill, New York.

SCHLICHTING, H. 1960 *Boundary Layer Theory*. McGraw-Hill, New York.

SHOHAM, O., BRILL, J. P. & TAITEL, Y. 1987 Two-phase splitting in a horizontal pipe tee-experiment and modeling. *Chem. Engng Sci.* **42**, 2667–2676.

SLIWICKI, E. & MIKIELEWICZ, J. 1988 Analysis of annular-mist flow model in a T-junction. *Int. J. Multiphase Flow* **14**, 321–331.

SQUIRE, H. B. & WINTER, K. G. 1951 The secondary flow in a cascade of aerofils in a non-uniform stream. *J. Aeronaut. Sci.* **18**, 271–277.

TRELA, M., ZEMBIK, J. & DURKIEWICZ, B. 1982 Droplet deposition on a flat plate from an air/water turbulent mist flow. *Int. J. Multiphase Flow* **8**, 227–238.

WALLIS, G. B. 1969 *One-dimensional Two-phase Flow*. McGraw-Hill, New York.

WARDLE, K. L. 1965 *Differential Geometry*. Dover, New York.

APPENDIX

The calculation of gas streamlines at the top and bottom walls in a horizontally oriented tee with a rectangular cross-section requires first the calculation of primary flow streamlines for the bulk flow away from the walls. Secondary flow components are then added to obtain wall streamlines. Secondary flow is produced due to viscous flow entering a curved path and producing a streamwise vorticity component. The calculational method derived herein is an extension of early analytical work on secondary flow by Squire & Winter (1951) and Hawthorne (1951) to boundary layer flow.

The vorticity transport equation may be derived directly from the Navier–Stokes equation (Currie 1974) as

$$(\mathbf{V}\cdot\nabla)\boldsymbol{\Omega} = (\boldsymbol{\Omega}\cdot\nabla)\mathbf{v} + \nu\nabla^2\boldsymbol{\Omega}, \qquad [A.1]$$

where

$\mathbf{V}$ = velocity,

$\boldsymbol{\Omega}$ = vorticity = $\mathbf{V}\times\mathbf{V}$

and

ν = viscosity.

If the magnitude of the velocity along a primary streamline in the bulk flow is given as V_0, with a coordinate system defined by the local streamline coordinate and its radius of curvature (figure A1), then the streamwise component of vorticity (ξ, in the s direction) is given by Horlock & Lakshminarayana (1973) as

$$\frac{\partial}{\partial s}\frac{\xi}{V_0} = \frac{2\eta}{V_0 R} + \frac{\nu}{V_0^2}\frac{\partial^2\xi}{\partial b^2}, \qquad [A.2]$$

where the vorticity components are:
streamwise (s direction),

$$\xi = \frac{\partial w}{\partial n} - \frac{\partial u}{\partial b}; \qquad [A.3]$$

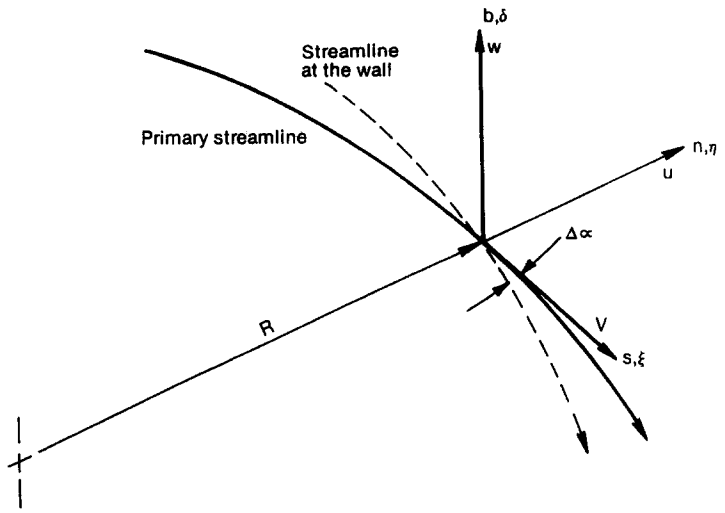

Figure A1. Streamline coordinates for wall streamline calculations.

normal (n direction),

$$\eta = \frac{\partial w}{\partial s} - \frac{\partial V}{\partial b}; \qquad [A.4]$$

and

binormal (b direction),

$$\zeta = -\frac{\partial V}{\partial n} - \frac{V}{R}. \qquad [A.5]$$

V is the magnitude of the velocity at (s, b) (V approaches V_0 away from the wall) in the primary flow direction. u and w are the secondary velocity components in the n and b directions, respectively, written in lower case to signify smaller magnitude than V. R is the scalar radius of curvature.

Within the wall boundary layer $w \cong 0$, and

$$\zeta = -\frac{\partial u}{\partial b} \qquad [A.6]$$

and

$$\eta = -\frac{\partial V}{\partial b}. \qquad [A.7]$$

Next, we examine the diffusion term in [A.2]. The Prandtl boundary layer equation for incompressible flow along a flat plate (Schlichting 1960) in the wall streamline direction is

$$V\frac{\partial V}{\partial s} + u\frac{\partial V}{\partial b} = \frac{-1}{\rho}\frac{\mathrm{d}P}{\mathrm{d}s} + \nu\frac{\partial^2 V}{\partial b^2}, \qquad [A.8]$$

where

ρ = density

and

P = pressure;

at the wall u, $V = 0$,

$$\nu\frac{\partial^2 V}{\partial b^2} = 0, \qquad [A.9]$$

applying L'Hospital's rule, with $V(s, b) = V_0(s)\, f(b)$ and $f(b) = b^{1/n}$, where $n \approx 7$ (Schlichting 1960), which fits our data well,

$$\lim_{V, b \to 0} \frac{\nu}{V^2} \frac{\partial^2 V}{\partial b^2} = \lim_{b \to 0} \frac{\partial^3 V}{\partial b^3} b^{(n-2)/n} = 0. \qquad [A.10]$$

For any $n \geqslant 2$.

Equation [A.2] may now be written

$$\frac{\partial}{\partial s}\left(\frac{\xi}{V_0}\right) = \frac{2\eta}{V_0 R}. \qquad [A.11]$$

Equation [A.1] may be integrated as

$$\frac{\xi}{V_0} = \int_0^s \frac{-2}{V_0 R} V_0 \frac{\partial f(b)}{\partial b}\, ds. \qquad [A.12]$$

The slope of the streamline at the wall with respect to the primary streamline at the coordinate of their intersection (ran α) is then

$$\tan \alpha = \lim_{b \to 0} \frac{u}{V} = \lim_{b \to 0} \frac{\dfrac{\partial u}{\partial b}}{\dfrac{\partial V}{\partial b}} \qquad [A.13]$$

$$= \frac{\xi}{V_0} \frac{\partial b}{\partial f(b)} = \int_0^s \frac{-2}{R}\, ds, \qquad [A.14]$$

where R is a function of s.